Article

Mg-Al Layered Double Hydroxide Doped Activated Carbon Composites for Phosphate Removal from Synthetic Water: Adsorption and Thermodynamics Studies

Abdelrahman K. A. Khalil [1,2] , **Fikri Dweiri** [2] , **Ismail W. Almanassra** [1] , **Anjaneyulu Chatla** [1,*] and **Muataz Ali Atieh** [1,3,*]

1   Research Institute of Sciences & Engineering (RISE), University of Sharjah, Sharjah P.O. Box 27272, United Arab Emirates; abdelrahman.khalil@sharjah.ac.ae (A.K.A.K.); ialmanassra@sharjah.ac.ae (I.W.A.)

2   Industrial Engineering and Engineering Management Department, College of Engineering, University of Sharjah, Sharjah P.O. Box 27272, United Arab Emirates; fdweiri@sharjah.ac.ae

3   Chemical and Water Desalination Engineering (CWDE) Program, College of Engineering, University of Sharjah, Sharjah P.O. Box 27272, United Arab Emirates

*   Correspondence: achatla@sharjah.ac.ae (A.C.); mhussien@sharjah.ac.ae (M.A.A.)

Abstract: Increased phosphate concentration in water bodies has led to eutrophication, and its removal is an inevitable requirement of sustainable wastewater purification systems. In this study, MgAl layered doubled hydroxide (LDH) composites doped on the surface of activated carbon (AC/MgAl LDH) with various (Mg + Al) total metal loading (5 wt%, 10 wt%, and 15 wt%) were prepared by the co-precipitation method. The influence of (Mg + Al) total metal loading onto AC was examined to remove phosphate ions from aqueous solutions. The effect of adsorption parameters, including adsorbent dosage, initial solution pH, initial phosphate concentration, contact time, and experiment temperature, were investigated via batch adsorption experiments. The adsorption results demonstrated that the phosphate adsorption capacity significantly improved with increasing the (Mg + Al) metal loading on the surface of AC. The maximum Langmuir phosphate adsorption capacity was 337.2 mg phosphate per gram of AC/MgAl-3 LDH composite (15 wt% Mg + Al) composite at pH ~6.3, 22 °C, and 1 g/L of adsorbent. The kinetic data were best fitted with the pseudo-second order model. The initial solution pH notably influenced the phosphate removal by AC/MgAl-3 LDH composite with a maximum removal at pH 2.3. According to the spent adsorbent characterization results, the dominant mechanisms of phosphate removal by AC/MgAl-3 LDH were electrostatic interactions, ion exchange, and inner-sphere complexation. The phosphate adsorption capacity was gradually increased with increasing the experiment temperature, suggesting an endothermic adsorption process. Overall, the AC/MgAl LDH composites pave the way for an effective strategy for phosphate removal from aqueous solutions.

Keywords: activated carbon; LDH composite; phosphate; adsorption; water treatment

1. Introduction

Providing fresh water is a crucial priority for the environment, animals, and humans. Water crises have been considered a significant challenge for different societies [1]. The use of treated wastewaters has reduced the stress on natural water resources. However, continuous population growth, industrialization, climate change, and the decrease in the sense of responsibility among humans for the quantity and kinds of waste disposed into the environment have led to the emergence of different kinds of pollutants in wastewater resources. All of this has resulted in increased stress on nature and the environment, as well as more challenges to wastewater purification systems. Scientific researchers are not far from responsibility and are working diligently to manufacture highly effective materials

to remove these pollutants. Moreover, they also constantly strive to improve the current purification technologies and develop new treatment technologies.

Among the different kinds of pollutants detected in wastewaters, nutrients such as phosphate and nitrate have received great attention due to their disastrous effect on water quality. Nutrients, mainly phosphate, are the main reason for water eutrophication. Phosphate exists in wastewater at high concentrations, and its residues were also detected in high levels in treated sewage effluent [2]. Phosphate is also a well-known fertilizer, and the extra use of phosphate in agriculture has resulted in the dissolution of phosphate with rainwater and its final discharge into the different surface and ground water resources. High phosphate levels can lead to algae blooms that cause algal poisons that harm human and animal health [3]. Therefore, working to develop materials to remove phosphates is one of the priorities to enable the full utilization of treated wastewaters.

Several methods have been investigated to remove the phosphates, including adsorption [4], coagulation [5], membrane processes [6], and ion exchange [7]. Among the recommended remediation technologies, adsorption has proven to be an effective way of removing contaminants while also allowing for the recycling of adsorbent materials [8]. Adsorption is a low-cost, environmentally friendly, easy-to-operate, effective, and desirable method [9]. Various materials were investigated for the elimination of phosphate from aqueous solutions such as silica gel [10], clays [11], AC [12], colloids [13], zeolites [14], carbon nanotubes [15], coals [16], and fly ashes [17]. The ACs were among the most used materials for phosphate removal due to their high surface area, chemical stability, and variety of functional groups [18]. Thus, its use was not limited to water treatment [19], but it has also been utilized in air and gas purification [20], ion exchange processes [21], catalysis [22], and the food industry [23].

In the last decade, layered double hydroxides (LDH) based anionic or hydrotalcite clay materials have gained more attraction for the uptake of all types of harmful anionic contaminants from wastewater. It compensates for the shortcomings of existing sorbents by providing high adsorption capacity, a simple preparation technique, reusability, and a low-cost value. LDHs could be used in various applications, including cation exchangers, catalysts, and the decontamination of organic and inorganic pollutants [24]. Gupta and Saifuddin et al. studied the removal of phosphate ions by Zn-Fe LDH synthesized by the co-precipitation method, the phosphate adsorption capacity was 36 mg P/g [25]. Santos et al. developed Mg-Fe-Cl LDH synthesized by the co-precipitation method for phosphate removal and they obtained a maximum adsorption capacity of 18.17 mg P/g [26]. Moreover, Liu and Zhang et al. prepared Mg/Al layered double hydroxide nanoparticles. The characterization results illustrated the formation of 4 to 6 LDH layers with a thickness of 3 to 5 nm, the maximum adsorption capacity was 98 mg P/g [27]. Research efforts are currently underway to use biochar and other low-cost waste-derived materials as effective adsorbents to decontaminate aqueous contaminants. Recentstudies reported that the LDHs doped carbonaceous materials could provide high adsorption capacity of phosphate [28,29]. The distribution of LDHs onto high surface area carbon-based materials substrates will decrease the amount of negative functional groups found on ACs in nature, and hence it will improve their affinity toward negatively charged pollutants such as phosphate.

The previous investigations of MgAl composites have led to the improved adsorption capacity of phosphate. However, so far, to the best of the authors knowledge, the removal of phosphate ions by Mg/Al composites doped onto the surface of AC derived from coconut shell has not been reported yet. Accordingly, the objectives of this work are to (1) apply the co-precipitation method to prepare AC/MgAl-LDHs composites of different (Mg + Al) total metal loading, (2) to investigate the influence of MgAl loading on the removal of phosphate from water, (3) to explore the effect of adsorption parameters on the removal of phosphate by the optimized loading of MgAl LDH onto AC, and finally (4) to propose the adsorption mechanism of phosphate by characterizing the phosphate loaded adsorbent.

2. Materials and Methods

2.1. Materials

Granular activated carbon type (AquaSorb® 2000) purchased from Jacobi Carbons Company (Kalamar, Sweden). A stock solution of 1000 mg/L PO_4^{3-} was prepared by dissolving potassium phosphate (KH_2PO_4) in DI H_2O, purchased from Honeywell Riedel-de Haën (Germany). NaOH pellets (Merck, Germany), Na_2CO_3 (Merck, Germany), $Mg(NO_3)_2 \cdot 6H_2O$ (Daejung, Korea), and $Al(NO_3)_3 \cdot 9H_2O$ (Sigma Aldrich, St. Louis, MO, USA) were used. The initial pH solution was controlled by adding NaOH (0.10 M) or HCl (0.10 M) purchased from Sigma Aldrich. All solutions were prepared with deionized (DI) water. All chemical/reagents were used as received without further treatment.

2.2. Synthesis of Activated Carbon & MgAl-LDH Composites

The modified co-precipitation method was used to prepare AC/MgAl-LDHs composites with different (Mg + Al) total metal loading (i.e., (Mg + Al-5 wt%, 10 wt% and 15 wt%) [30]. Briefly, an aqueous metal solution was prepared by dissolving $Mg(NO_3)_2 \cdot 6H_2O$ and $Al(NO_3)_3 \cdot 9H_2O$ in 300 mL DI water under vigorous stirring, then 20 g of AC was added into the metal aqueous solution. The metal solution pH-11 was adjusted using a 1.0 mol/L NaOH aqueous solution. The prepared black AC with the aqueous solution aged for 2 h at 60 °C. The obtained precipitation was filtered and washed with DI water four times. Finally, the obtained AC-supported MgAl-LDH composites were then dried in the oven at 100 °C for 24 h. The prepared AC/MgAl-LDH composites were denoted as AC/MgAl-1 (Mg + Al-5 wt%), AC/MgAl-2 (Mg + Al-10 wt%) and AC/MgAl-3 (Mg + Al-15 wt%) in the current study.

2.3. Characterization of AC/MgAl LDH Composites

The BET surface area, total pore volume, and average pore size were measured by the nitrogen adsorption-desorption process at −196 °C using the NOVATECH LX2 analyzer, Anton Paar. Before the N_2 analysis, the sample was degassed at 300 °C for 6 h. Field Emission Scanning Electron Microscopy (Thermo scientific Apreo C FESEM, Waltham, MA, USA) was used to visualize the microstructure and morphology of the prepared material in secondary electron mode. The FESEM is equipped with an energy dispersion spectrometer (EDS), which was employed to investigate the elemental mapping of the AC/MgAl before and after adsorption. The SEM/EDS accelerating voltage was 15 kV. The crystallinity of the composites was investigated by X-ray diffractometer (XRD, Bruker, D8 Advance, Bremen, Germany) with a Cu Kα having wavelength λ = 1.54056 Å as an X-ray source at a generator voltage of 40 kV and a generator current of 40 mA. Infrared spectra of AC/MgAl LDH composites were obtained using a Jasco FT-IR (Model 6300 instrument, Japan), the spectra was recorded between 4000 and 400 cm^{-1}. The chemical composition of the AC/MgAl samples was obtained by using X-Ray Fluorescence Spectrometer (Horiba scientific XGT-7200, Kyoto, Japan).

2.4. Batch Adsorption Experiments

Adsorption tests were carried out in batch mode. The AC/MgAl was added to 20 mL of phosphate solution in 50 mL glass Erlenmeyer flasks and shaken under the proper conditions in a Kuhner Lab-Shaker LS-X (Model MAZ10661LAB, San Carlos, CA, USA). High-temperature experiments were conducted by JEIO TECH Incubated Shaker (Model ISF-7100R, Daejeon, Korea). Samples for examination were collected, and phosphate content was measured using ion chromatography (Thermo Scientific™ Dionex ICS-5000 Ion Chromatography). A calibration curve was created for IC calibration and quantification by examining a standard of known phosphate concentrations. The adsorption capacity Q (mg of phosphate/g) and removal efficiency (*RE*, %) were calculated according to Equations (1) and (2) [31].

$$Q = \frac{(C_i - C_e) \times V}{W} \tag{1}$$

$$RE(\%) = \frac{(C_i - C_e)}{C_i} \times 100 \tag{2}$$

where C_i and C_e are the initial and final phosphate concentrations (mg/L), respectively, V is the phosphate solution volume (L), and W is the AC/MgAl mass (g). Each adsorption test was repeated twice, and average values were represented. The removal efficiency of phosphate on raw AC, AC/MgAl-1, AC/MgAl-2, and AC/MgAl-3 was studied to choose the optimum adsorbent of AC/MgAl composites at the following conditions (Dose; 1.5 g/L, temp; 22 °C, pH; 6.5). The effect of AC/MgAl dosage was investigated using AC/MgAl amounts ranging from 0.2 to 2 g/L. The initial pH of the phosphate solution was adjusted between 2 and 12. The effect of temperature on adsorption thermodynamics was studied by varying the feed temperature from 295 to 333 K. All experiments except the effect of pH were performed at as prepared pH 6.3 using an agitation speed of 200 rpm. The equilibrium time was 24 h and considered for all the experiments. The pH drift method investigated the zero point of charge (ZPC) for raw and the optimized adsorbent. Briefly, 20 mg of each material was added to 20 mL of 0.1 M NaCl at different pH values between 2 and 12. The initial pH was adjusted by adding 0.1 M NaOH or HCl droplets. Next, the suspensions allowed for shaking for 72 h, and the pH_f was measured and recorded.

2.5. Adsorption Modeling

2.5.1. Isotherm

To investigate the fitting of experimental data with different isotherms models, 20 mg of AC/MgAl were added to a volume of 20 mL of phosphate solution with concentrations ranging between 20 and 1000 mg/L at 22 °C, agitation speed of 200 RPM, and pH 6.3 for 24 h. The adsorption isotherm data were analyzed using Langmuir [32], Freundlich [33], and Sips [34] isotherm models. The parameters and expressions of the model are listed in Table 1.

Table 1. List of the isotherm models, mathematical equations, and related parameters.

Isotherm Model	Mathematical Equation	Related Parameters
Langmuir	$q_e = \frac{X_m h C_e}{(1 + h C_e)}$	X_m, Langmuir maximum surfactant capacity (mg/g). h, Langmuir constant (L/mg)
Freundlich	$q_e = K_F C_e^{\frac{1}{n_F}}$	K_F, Freundlich adsorption capacity coefficient $\frac{mg}{g \cdot \left(\frac{mg}{L}\right)^{1/n_F}}$ and n_F coefficient of adsorption intensity
Sips	$q_e = \frac{Q_s K_s C_e^{n_s}}{1 + K_s C_e^{n_s}}$	Q_s and K_s Sips model constants (L/g and L/mg, respectively), n_s Sips model exponent.

The Langmuir adsorption model assumes that one layer of the pollutant will cover the adsorbent's surface [35]. The equilibrium parameter of the Langmuir model (R_L) can be used to decide whether the adsorption process is favorable or not. The adsorption is favorable if R_L is between 0 and 1, linear if $R_L = 1$, unfavorable if $R_L > 1$, and irreversible if $R_L = 0$ [36]. R_L can be determined using Equation (3) [37].

$$R_L = \frac{1}{1 + h C_0} \tag{3}$$

where C_0 denotes the initial concentration of phosphate.

The Freundlich isotherm model is typically used to describe non-ideal, reversible, and heterogeneous systems in which (1) adsorption is not confined to a monolayer coverage and (2) adsorption capacity rise as feed adsorbate concentration increases. The three-parameter Sips model is useful in the range between the Freundlich and Langmuir isotherms. The Sips model is more useful for understanding heterogeneous systems. These isotherms were

used to investigate the equilibrium data using the Excel solver by minimizing the sum of squared errors (*SSE*), which can be determined using Equation (4) [36].

$$SSE = \sum_{i=1}^{n} \left(q_{i(exp)} - q_{i(cal)} \right)^2 \tag{4}$$

where $q_{i(exp)}$ and $q_{i(cal)}$ are the experimental and model-estimated adsorption capacities (mg/g), respectively, n is the number of data points.

2.5.2. Kinetics

Adsorption kinetics modeling was investigated to understand the adsorption dynamic mechanism of phosphate adsorption onto AC/MgAl LDH composites [38]. The data were analyzed to examine the rate determining step of the adsorption process and summarize the adsorption capacity of AC/MgAl LDH composites [39]. The experimental data were considered using the adsorption kinetic models recorded in Table 2. The table shows the linearized states of the kinetic models utilized to analyze the experimental data. The experiment was conducted using 200 mg AC/MgAl LDH composites with 200 mL of phosphate solution (50 mg/L phosphate, pH 6.3) in a 200 mL glass Erlenmeyer flask. The intervals were chosen as (1, 5, 15, 30, 60, 180, 360, and 1440 min).

Table 2. List of kinetic adsorption models, description, and nomenclature.

Kinetic Model	Linearized Form	Nomenclature	Ref.
Lagergren pseudo-first order	$log(q_e - q_t)$ $= log(q_e) - \left(\frac{k_1}{2.303}\right)t$	q_t and q_e are the amounts of PO_4^{3-} adsorbed by AC/MgAl composites (mg/g) at certain time t(min). k_1 is the pseudo-first order rate constant (min^{-1}).	[40]
Ho-McKay pseudo-second order	$\frac{t}{q_t} = \frac{1}{k_2 q_e^2} + \left(\frac{1}{q_e}\right)t$	k_2 is the constant of the pseudo-second order model (g/mg/min).	[41]
Elovich	$q_t = \frac{1}{\beta}\ln(\alpha\beta) + \frac{1}{\beta}\ln t$	α is the adsorption rate at the beginning of the process (mg/g/min), β is the desorption constant (g/mg).	[42]
Intra-particle diffusion	$q_t = k_{ip} \times SQRT(t) + c$	k_{id} is the constant of the intra-particle diffusion $(mg/g/min^{-0.5})$, c is a constant connected to the boundary layer thickness (mg/g).	[43]

where SQRT represents the square root.

2.5.3. Thermodynamics

The three thermodynamic parameters, i.e., standard Gibbs free energy $\Delta G°$, standard enthalpy $\Delta H°$, and standard entropy $\Delta S°$, were determined to assess the spontaneity, mechanism, and feasibility of the adsorption process. $\Delta G°$ was determined according to Equation (5).

$$\Delta G° = -RT \ln K_d \tag{5}$$

where R was the gas constant, T was the temperature in Kelvin, and K_d was the adsorption process' thermodynamic equilibrium constant. K_d is determined by Equation (6).

$$K_d = \frac{C_a}{C_e} \tag{6}$$

where C_a is the adsorbed amount of phosphate onto the AC/MgAl at equilibrium (mg/L).

The entropy and enthalpy changes can be evaluated by plotting $\ln K_d$ versus $(1/T)$ using the Van't Hoff equation (Equation (7)).

$$\ln K_d = \frac{\Delta S^\circ}{R} - \frac{\Delta H^\circ}{RT} \tag{7}$$

3. Results and Discussion

3.1. Characterization of AC/MgAl-LDH Composite Adsorbents

The physicochemical properties of the prepared AC/MgAl LDH composites adsorbents are listed in Table 3. The elemental compositions of AC/MgAl LDH composites were estimated by X-ray fluorescence spectroscopy (XRF). The obtained results indicate that XRF elemental composition values are well matched with theoretical values. Morphology of the AC/MgAl LDH composites was analyzed using FESEM-EDS analysis, and the corresponding images and EDS spectrum were presented in Figure 1. Figure 1a shows FESEM image of raw AC, it can be seen that raw AC contains high porous nature with a wide pore radius size and the EDS mapping confirms the carbon as the main composition with a little amount of Si. As shown in Figure 1b, AC/MgAl-1 displayed a rough surface with irregular shape particles, while AC/MgAl-2 and AC/MgAl-3 showed a smooth surface covered by spherical particles (see Figure 1c,d). Furthermore, the EDS spectrum of all the AC/MgAl LDH composites presented carbon, Mg, Al, and oxygen elementals as illustrated in Figure 1b–d. The EDS analysis results confirm the successful incorporation of (Mg + Al) elements into AC matrices and which is further confirmed by XRD analysis.

Table 3. XRF elemental composition, BET surface area, and total pore volume of AC/MgAl LDH composites.

Sample	[1] Elemental Composition Mg:Al (Molar Ratio)	BET Surface Area (m²/g)	Total Pore Volume (cm³/g)
Raw AC	-	829.596	0.478
AC/MgAl-1	0.028:0.012	742.078	0.487
AC/MgAl-2	0.061:0.029	656.762	0.448
AC/MgAl-3	0.085:0.035	584.124	0.441

[1] Estimated from XRF analysis.

The prepared AC/MgAl LDH composite's surface area, pore volume, and pore radius were calculated using the N_2 adsorption/desorption method. Figure 2 shows the N_2 adsorption/desorption isotherms of raw AC, AC/MgAl-1, AC/MgAl-2, and AC/MgAl-3 LDH composites. According to the International Union of Pure and Applied Chemistry (IUPAC) classification, raw AC and AC/MgAl composites presented type II isotherm with microporous nature [44], whereas high (Mg + Al) metal content AC/MgAl-2, and AC/MgAl-3 composites exhibited a typical type IV adsorption isotherm with an H_3 hysteresis loop, demonstrating the typical mesoporous nature materials [45] which could be probably due to the incorporation Mg and Al into AC matrices thus might expand the porosity of parent AC material. Table 3 presents the BET surface area, total pore volume of raw AC, AC/MgAl-1, AC/MgAl-2, and AC/MgAl-3 LDH composites. The samples show a gradual decrease in the BET surface area from 829.596 to 584.124 m²/g while increasing the (Mg + Al) metal loading because a high quantity of Mg/Al-LDH may cause pore blockages in AC, resulting in a decline in the surface area to 584.124 m²/g. The surface area observations are also corroborated with the pore volumes of the raw AC and AC/MgAl LDH composites.
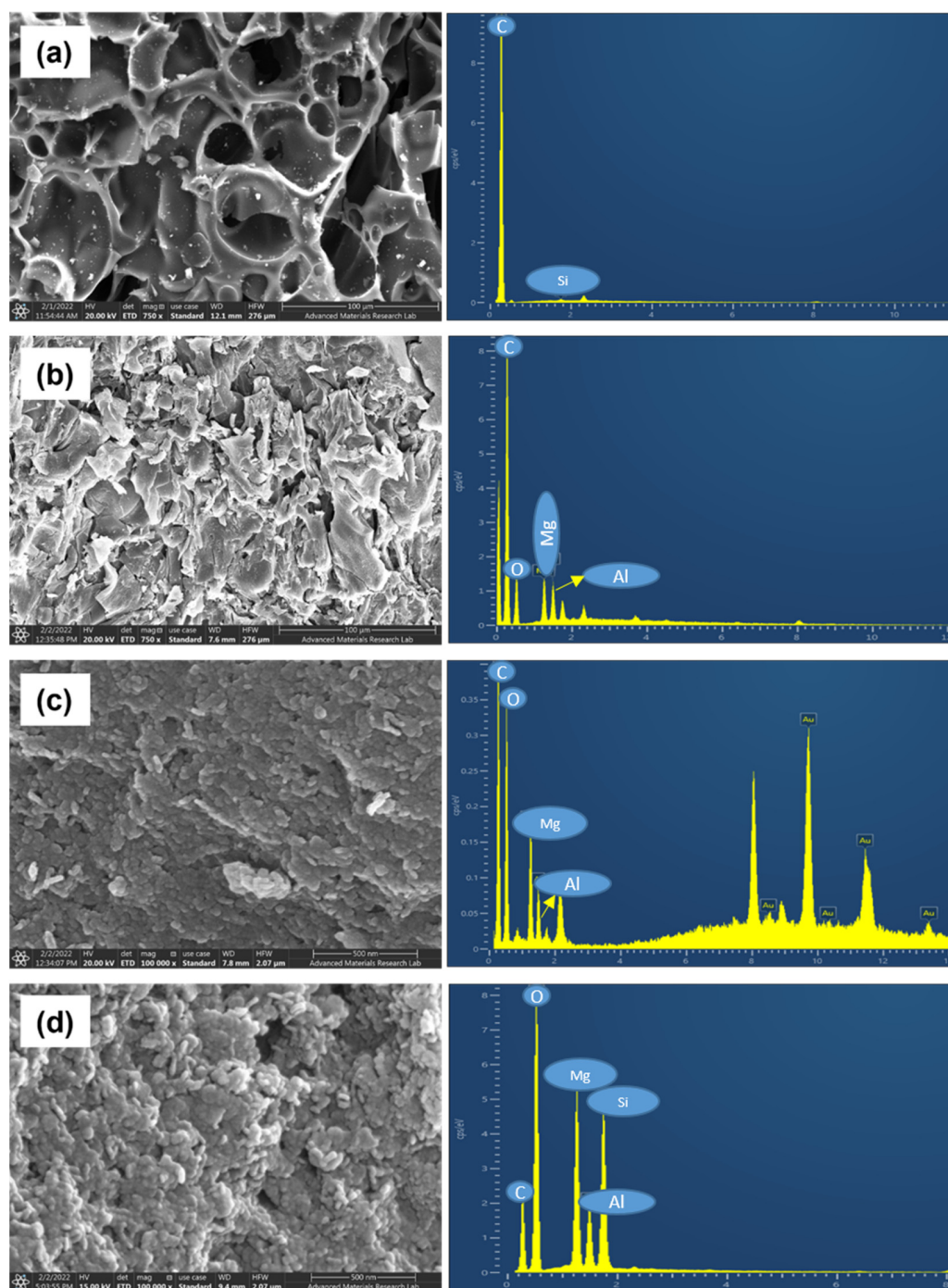
Figure 1. FE-SEM images of (**a**) raw AC, (**b**) AC/MgAl-1, (**c**) AC/MgAl-2, and (**d**) AC/MgAl-3 LDH composites.

The FT-IR spectrum of the AC/MgAl LDH composites adsorbents with different (Mg + Al) metal loading is illustrated in Figure 3. The bands located at 3457 cm^{-1} and 1648 cm^{-1} are ascribed to -OH stretching and bending vibration [46]. The peak detected at 2367 cm^{-1} is assigned to the stretching vibration of atmospheric CO_2 [47]. In addition, the peak at 2930 cm^{-1} was assigned to C-H stretching vibration of AC material [48]. However, Mg + Al content composites displayed a sharp peak at 1401 cm^{-1} is assigned to the typical nitrate ($NO_3{}^{2-}$) substances between the LDH interlayers [49]. In contrast, the absorption peak at 1097 cm^{-1} is attributed to the C-O stretching modes of AC [50]. The peaks between 500 and 800 cm^{-1}, including 633 and 804 cm^{-1} assigned to stretching

vibrations of metal oxide bonds such as M-O and O-M-O [50–52]. The presence of MgAl-LDH characteristic peak at 1401 cm^{-1} in AC/MgAl-LDH composites demonstrates the LDH structure formation in the AC matrixes. The FT-IR results indicate that the surface of the AC/MgAl LDH adsorbents possessed a higher content of oxygen-containing groups, which could significantly enhance the adsorption performance.
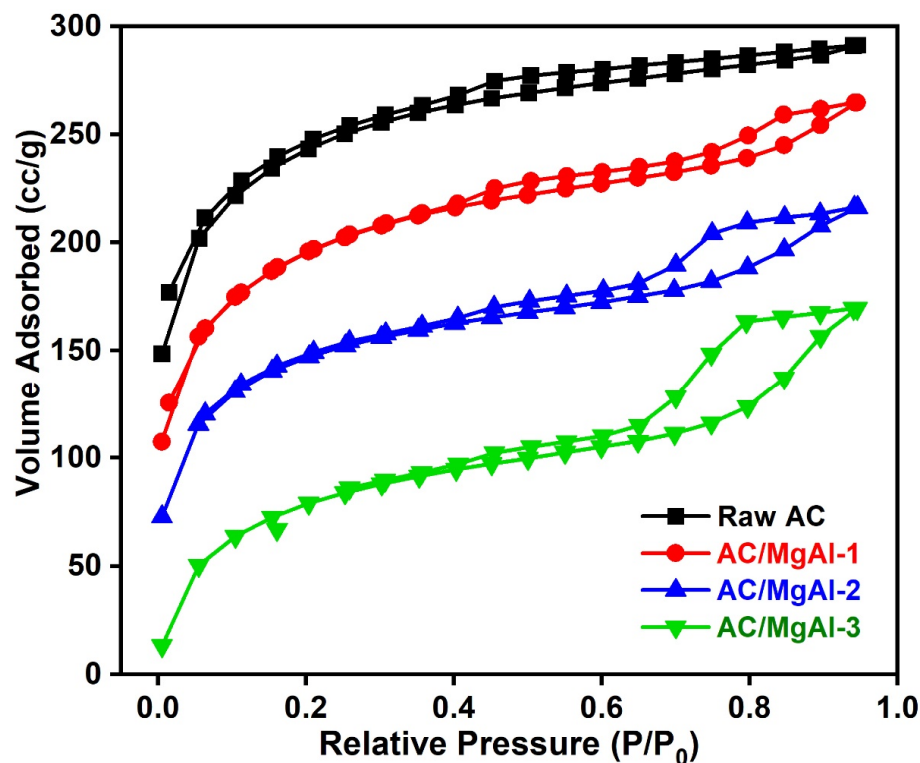

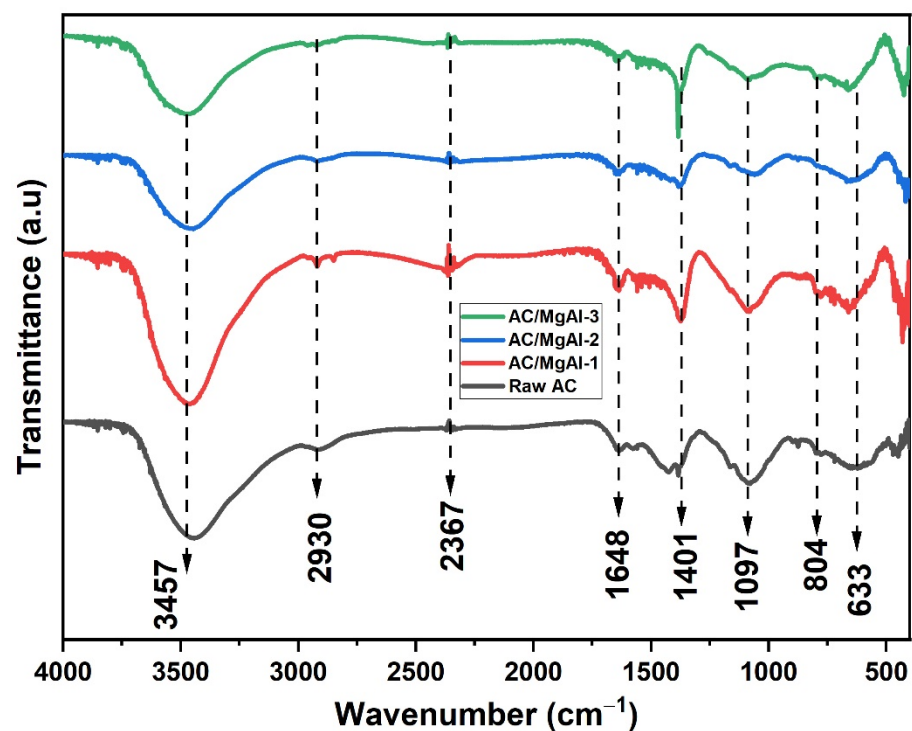**Figure 2.** N$_2$ adsorption/desorption isotherms of AC/MgAl LDH composites.

Figure 3. FT-IR spectra for AC/MgAl LDH composites.

XRD patterns of the raw AC, AC/MgAl-1, AC/MgAl-2, and AC/MgAl-3 composites are shown in Figure 4. The raw AC displayed a sharp diffraction peak at 2θ = 26.75°, corresponding to the (002) plane of the graphitic structure of carbon [37]. For AC/MgAl LDH composites, in addition to the graphitic carbon, some new diffraction peaks were noticed at 2θ = 11°, 23°, and 34° with (003), (006), and (012) planes attributed to the typical LDH structure of MgAl. These diffraction peaks are associated with the R3m rhombohedral symmetry of the MgAl LDH [53]. Moreover, the results confirmed that Mg/Al-LDHs were successfully incorporated into the AC matrix.
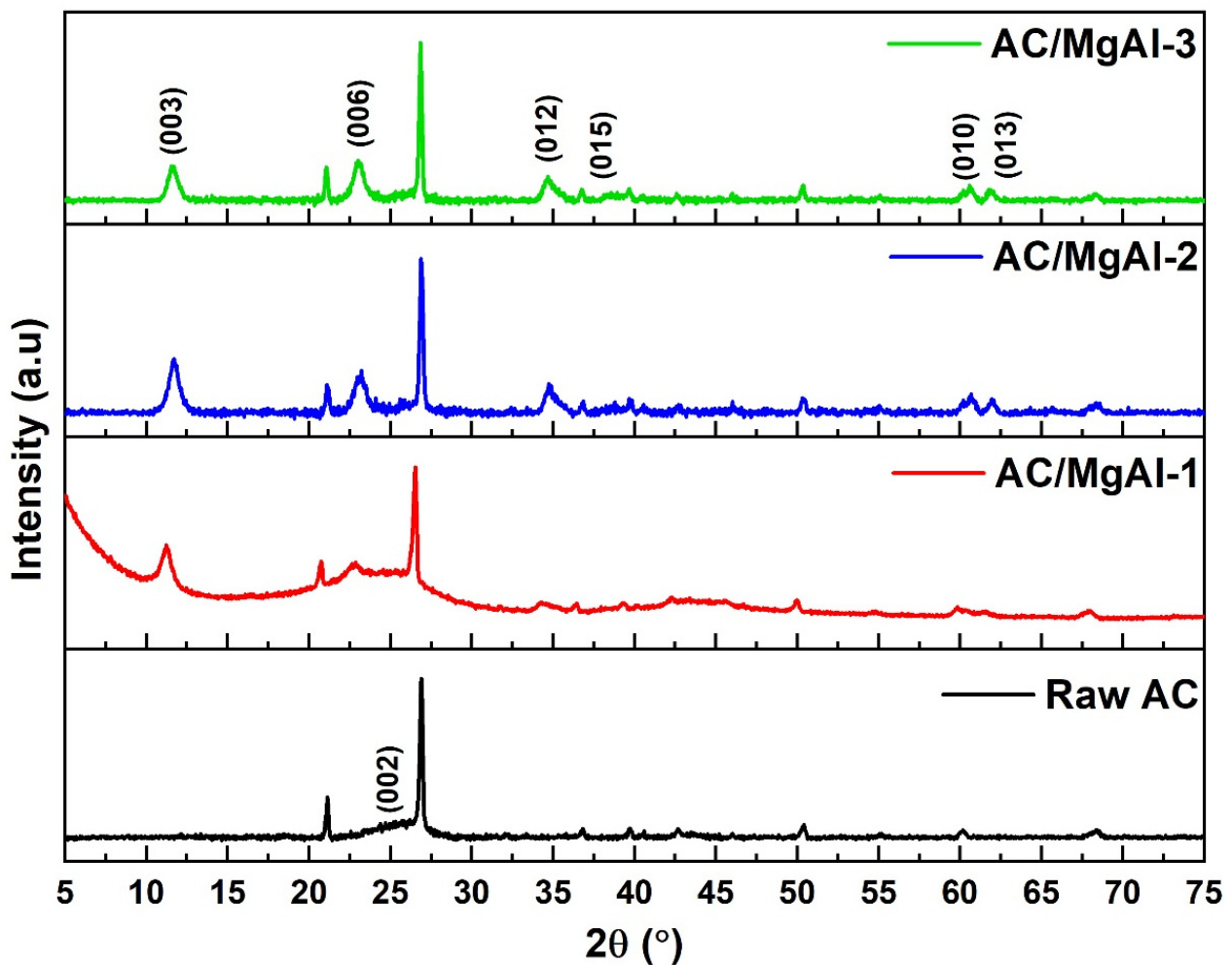

Figure 4. XRD patterns of AC/MgAl LDH composites.

3.2. Preliminary Adsorption Study

A preliminary adsorption study was performed to select the ideal MgAl metal loading on the surface of AC for the adsorption of phosphate ions. Figure 5 depicts the influence of MgAl loading on the adsorption capacity of phosphate. The adsorption results demonstrated a significant improvement in the adsorption capacity of phosphate by increasing the MgAl loading. For instance, the adsorption capacity was 8.5 mg/g for raw AC, 10.1 mg/g for AC/MgAl-1, 18.2 mg/g for AC/MgAl-2, and 20.8 mg/g for AC/MgAl-3. The increase in the adsorption capacity with MgAl metal loading is attributed to the affinity of MgAl composite toward phosphate ions. Moreover, the increase in adsorption capacity with MgAl metal loading is attributed to the higher amount of MgAl nanoparticles, which offer more positively charged adsorption sites and increased adsorption capacity. Based on these results, the AC/MgAl-3 was chosen as the optimum adsorbent for the rest of the adsorption experiments.
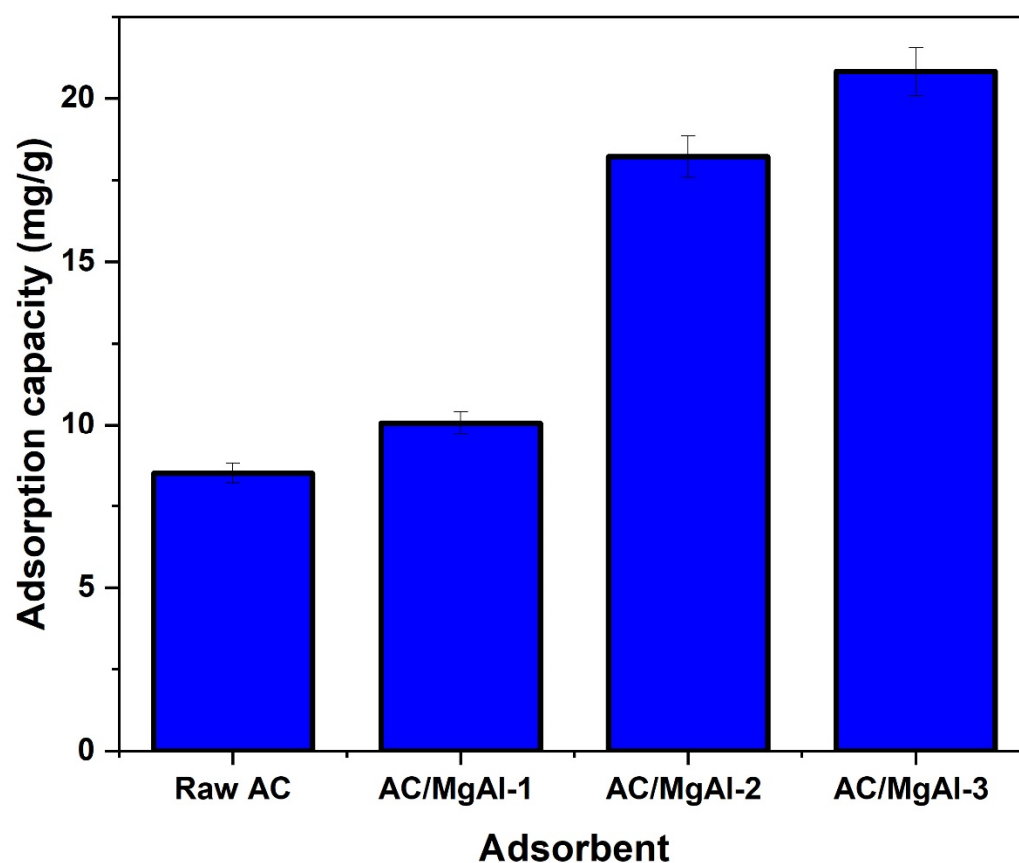
Figure 5. The effect of adsorbent type on phosphate adsorption capacity, pH = 6.3, C_0 = 50 mg/L, T = 22 °C.

3.3. Effect of Adsorbent Dose

The influence of AC/MgAl-3 dosage on the removal efficiency and adsorption capacity of phosphate is illustrated in Figure 6. It is noticed that the phosphate removal efficiency increased with increasing the AC/MgAl-3 dosage against a fixed initial phosphate concentration. These results are explained by the fact that increasing the adsorbent amount will provide more contact surface area and more adsorption sites, and hence the removal increases. In contrast, the adsorption capacity decreased with increasing the adsorbent dosage, which is attributed to the inverse relationship between the adsorption capacity and the mass of the adsorbent [54]. For economic purposes and to optimize both the adsorption capacity and removal efficiency, the intersection point of adsorption capacity and removal efficiency (around 1 g/L) is recommended to remove phosphate by AC/MgAl-3 and used for the rest of the study.

3.4. Effect of Initial pH on Phosphate Adsorption

For phosphate removal from aqueous media, the pH is one of the most critical parameters as it controls the adsorbent's surface charge and phosphate dissociation chemistry. The experimental data on the effect of pH on phosphate removal by AC/MgAl-3 are illustrated in Figure 7. It can be seen from Figure 7 that phosphate removal declined from 90% to 50% by raising the pH from 2 to 11. Moreover, the removal was almost stable at neutral conditions between pH 6.3 and 8.3. Accordingly, the removal of phosphate ions is favorable in acidic conditions, and the adsorption performance was impaired in the basic media. As a result, the initial solution pH 2.3 is considered an optimum value for removing phosphate ions by AC/MgAl-3. Similar behavior of the effect pH on phosphate removal was reported in the literature [55]. It was revealed that the results were cross-linked with the acid-base characteristics/charge of the AC/MgAl-3 adsorbent and phosphate ions dissociation in the

solution at various pH values. The phosphate ions dissociate with pH and form several forms of phosphate H_3PO_4, $H_2PO_4^-$, HPO_4^{2-}, and PO_4^{3-} [56].
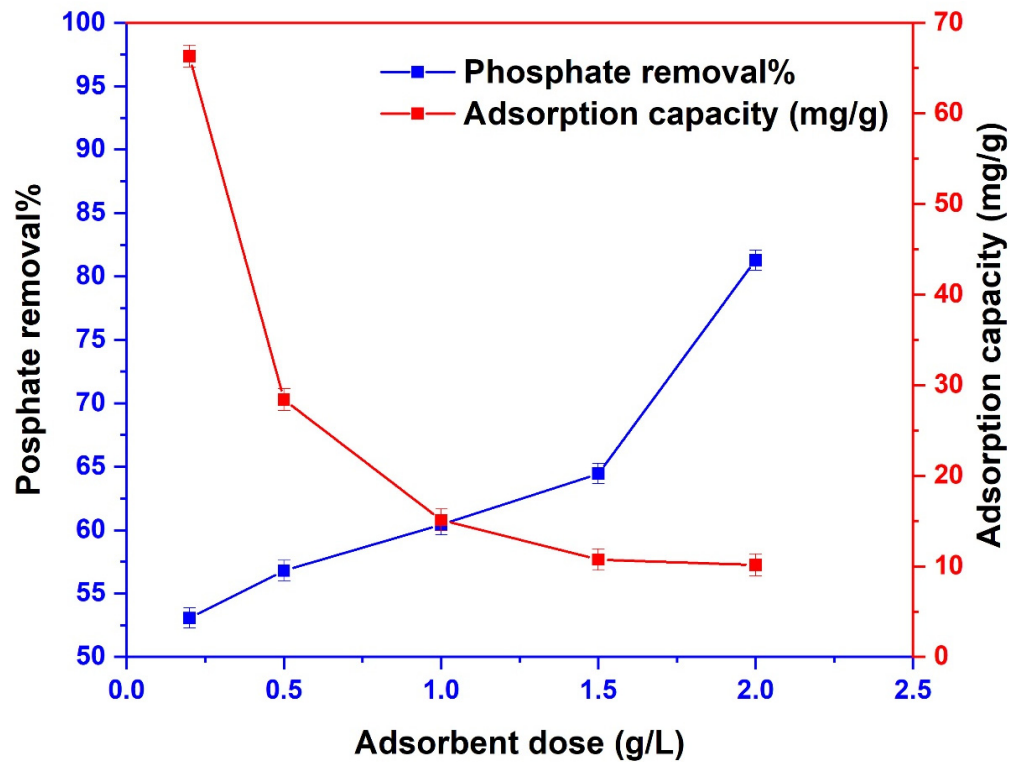

Figure 6. The effect of AC/MgAl-3 dosage on the removal efficiency and adsorption capacity of phosphate.
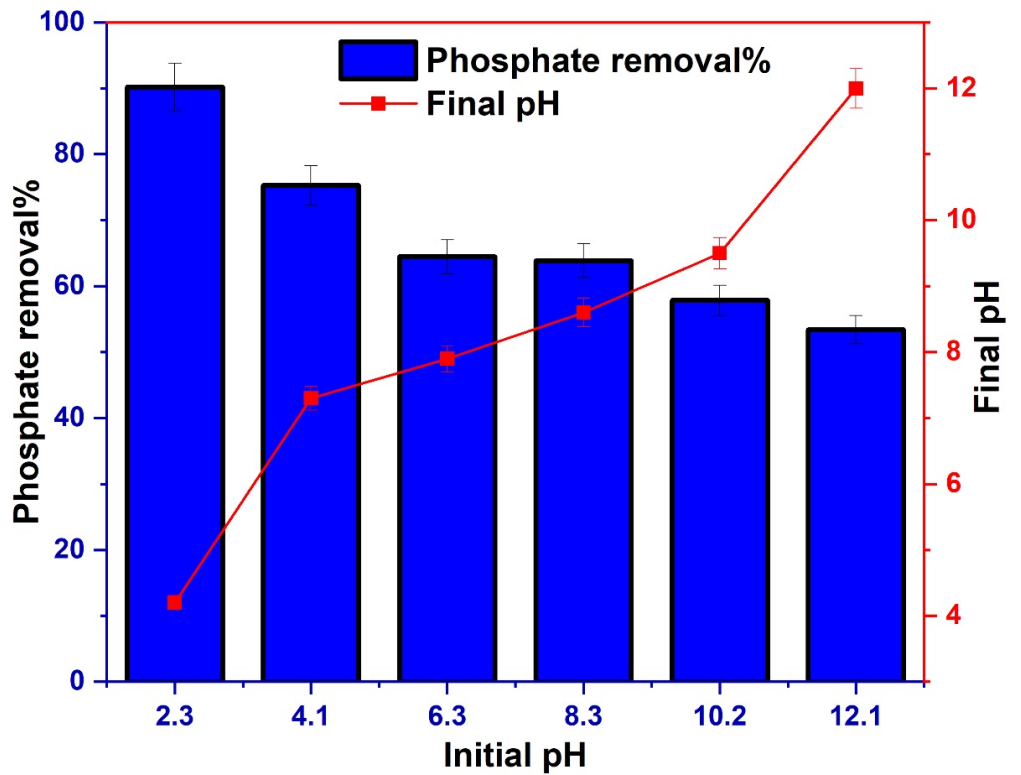

Figure 7. Effect of initial pH on the removal efficiency of phosphate and final pH.

The ZPC relates to the mechanism of adsorption and defines the situation in which the density of the electrical charge [57]. When the pH of the solution is less than the ZPC value, the adsorbent's surface charge is positive, enabling the anions to be adsorbed. If the pH is higher than the ZPC value, the surface charge of the adsorbent will be negative, allowing higher adsorption of cations [57]. The ZPC of the AC/MgAl-3 was observed to be around 9.2, as demonstrated in Figure 8. The influence of pH can be explained as follows, at pH 2.3, phosphate exists mostly as $H_2PO_4^-$ and it is getting adsorbed by highly positive adsorbent by the strong electrostatic interactions leading to removal efficiency of 90.2%. At pH 4.1, phosphate ions exist as $H_2PO_4^-$ and the magnitude of the positive charge of the adsorbent decreased, and hence the degree of the electrostatic interactions declined by raising the pH to 4.1, which in turn resulted in decreased removal efficiency to about 75.3%. At pH 6.3, the surface charge of the adsorbent is decreased, and the phosphate ions exist as a mixture of $H_2PO_4^-$ and HPO_4^{2-}, but mostly as $H_2PO_4^-$, while at pH 8.3, the magnitude of positive surface charge is expected to decrease and phosphate ions exist mostly as HPO_4^{2-} [58]. Therefore, the removal efficiency decreased to 64.4% and 63.9% at pH 6.3 and 8.3, respectively, due to the reduction in the magnitude of the electrostatic interactions [56,59].
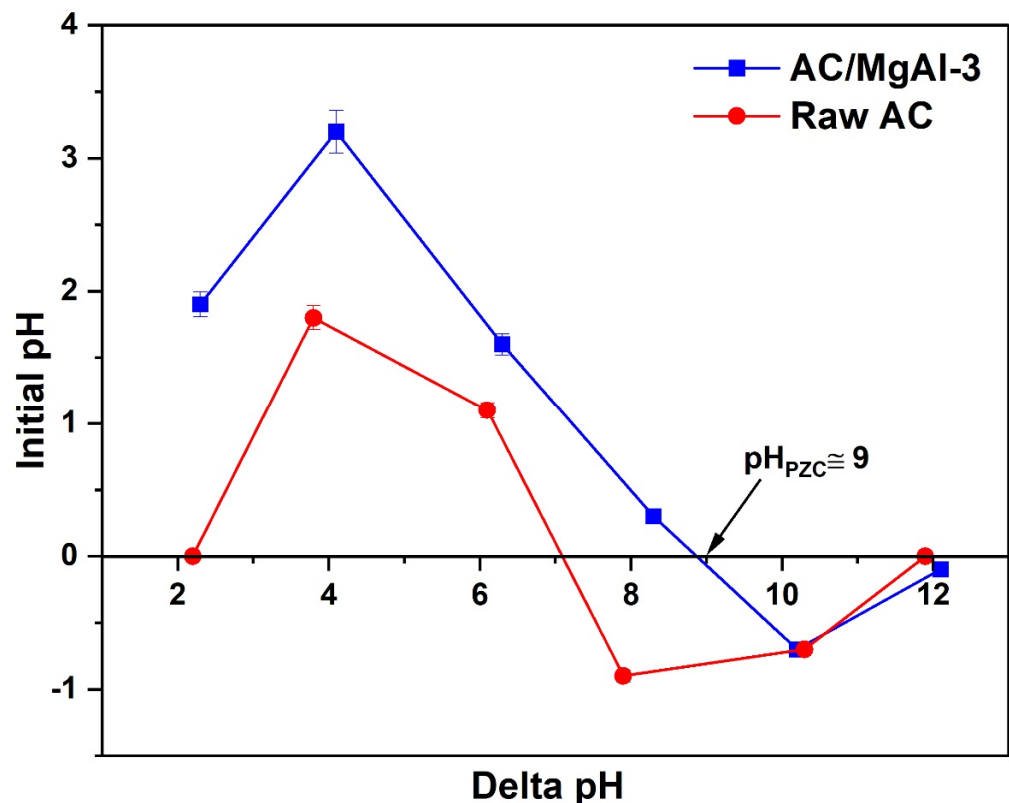

Figure 8. ZPC of raw AC and AC/MgAl-3 determined using the pH drift method.

At pH 10.2, the adsorbent becomes negatively charged as the ZPC is 9.2, suggesting that no more electrostatic interactions exist in the adsorption process. In contrast, the electrostatic repulsions control the interactions between phosphate ions and the adsorbent surface, and hence the removal decreased to 57.8%. Moreover, increasing the pH to 10.2 implies that the hydroxide ions concentration increases, which in turn competes with phosphate ions on the active adsorption sites, and hence the overall removal efficiency decreased. Further increasing the pH to 12.1 will increase the magnitude of electrostatic repulsions and the concentration of hydroxide ions, and hence the removal is decreased to 53.4%. It is worth mentioning that still, more than 53% removal is achievable at very basic conditions, which is attributed to the affinity of MgAl LDH toward phosphate ions.

3.5. Adsorption Isotherm

Figure 9 depicts the phosphate adsorption isotherms on AC/MgAl-3 at room temperature and at initial concentrations ranging from 20 to 1000 mg/L. The generated isotherm curves were non-linearly optimized using the Excel solver. It is clear that when the initial concentration of the phosphate increases, the phosphate adsorption capacity increases rapidly before gently reaching a plateau.
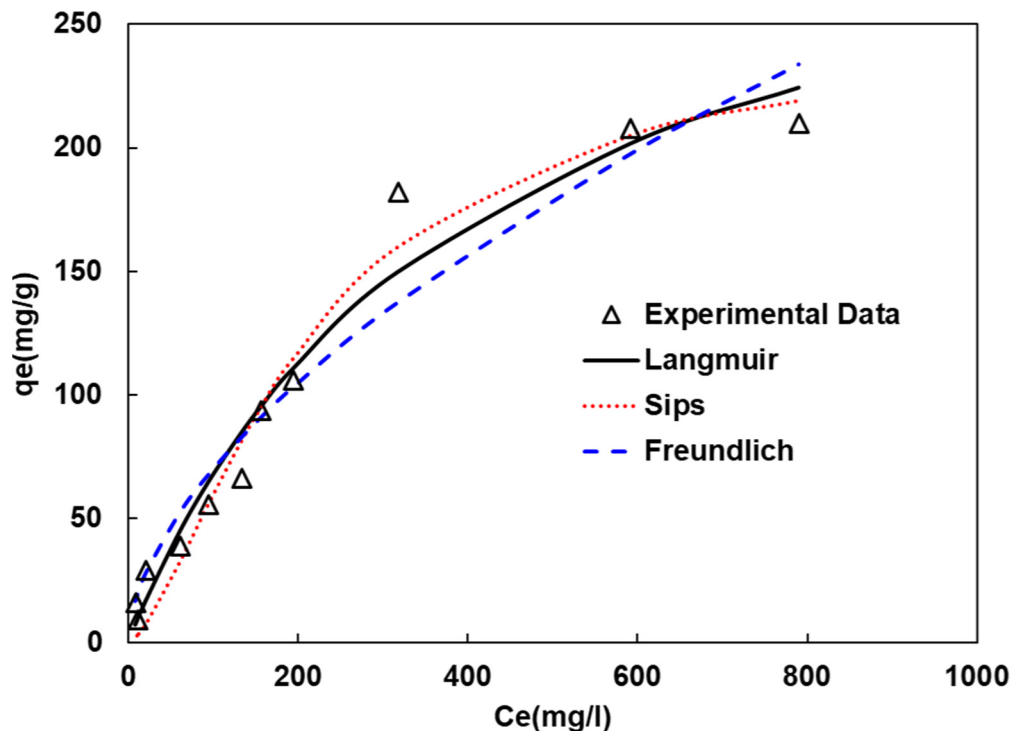

Figure 9. Nonlinear isotherms fitting of phosphate removal by AC/MgAl-3.

The model's parameters and statistical analysis of each fitted model are presented in Table 4, and the nonlinear fitting plots of the tested isotherms are illustrated in Figure 9. According to Figure 9, the Sips model provides the most accurate description of the experimental data. This is confirmed by the highest R^2 (0.969) and the lowest SSE (1643) values. However, the values of R^2 and SSE obtained for the Langmuir model are slightly better than the Freundlich model (see Table 4). Accordingly, the adsorption process of phosphate ions onto AC/MgAl-3 is controlled by both heterogeneously and homogeneously distributed binding sites, implying that monolayer and multilayer adsorption processes occurred in the removal process.

Table 4. Determined isotherm parameters for phosphate adsorption on AC/MgAl-3.

Model	Parameters		Adj. R^2	SSE
Langmuir	X_m (mg/g)	337.2	0.9598	2013.34
	h (L/mg)	0.003		
Freundlich	K_f	4.8	0.95278	3423.66
	n_F	1.72		
Sips	K_s (L/mg)	0.0003	0.96946	1643.32
	n_s	1.5		
	Q_s (L/mg)	250.8		

The Freundlich coefficient n_F is greater than 1, indicating that AC/MgAl-3 effectively removes phosphate ions. The number $1/n_s$ in the sips model indicates the heterogeneity of the AC/MgAl-3 active sites. If $1/n_s$ is equal to or near 1, the adsorption site is homogeneous, but if it is significantly more than 1, the adsorption site will be heterogeneous. The $1/n_s$ value observed in this study is less than 1, showing that AC/MgAl-3 adsorption sites towards phosphate are more homogenous, confirming the R^2 and *SSE* values. The experimental maximum adsorption capacity for phosphate onto AC/MgAl-3 was 209.8 mg/g, while the Langmuir adsorption capacity was found to be 337.2 mg/g. Both capacities were considered among the best for phosphate ions removal by different LDHs listed in Table 5. The R_L values in the Langmuir model were between 0.28 and 0.95, indicating that this adsorption process is favorable. Accordingly, the AC/MgAl composite could be a promising adsorbent of phosphate in real wastewater treatment.

Table 5. Comparison of different reported adsorbents for adsorption of phosphate.

Adsorbent	pH	Dosage (g/L)	PO_4^{3-} Concentration (mg/L)	Adsorption Capacity (mg(PO_4^{3-})/g)	Ref.
MgAl LDH nanoparticles using urea as a dispersing agent	8.5	1	30–360	300	[27]
4:1 Mg/Al-LDHs biochar	3	2.5	15–1500	81.83	[30]
[Zn-Al]-LDH	7	-	112.64–4505.60	348.21	[60]
Magnetic Fe_3O_4@MgAl-LDH@La(OH)3	7	0.1	18–36	199.5	[61]
AC/MgAl LDH composite	6.5	1	20–1000	337.2	Current study
Mg/Al LDH	3	0.6	30–15,000	213.6	[62]
BBAC@Zn–Al LDH	-	2	-	87.004	[63]
CuAl/CF-LDH	8	0.2	25–1500	100	[64]

3.6. Kinetics

Figure 10 illustrates the adsorption kinetics of phosphate ions onto AC/MgAl-3. As depicted in Figure 10, the rate of phosphate adsorption was initially rapid (in the first 60 min) due to the availability of vacant sites and the high concentration gradient between the adsorbent surface and the bulk solution. In this period, more than 50% of the phosphate was removed. Next, the removal rate has decreased between 60 and 1000 min, in which the adsorption occurs in the microporous and mesoporous structure of the adsorbent. Finally, after 1000 min, the adsorbent is saturated with phosphate ions, and equilibrium has been achieved, hence there are no major changes in the adsorption capacity.

The results of adsorption kinetics are consistent with previous investigations of phosphate removal by LDHs [10,65]. Perhaps the electrostatic interaction between the positively charged metal oxide surfaces and the negatively charged phosphate ions is responsible for the initial high rate of adsorption in this experiment. To further investigate the nature of the removal mechanism, the pseudo-first order, pseudo-second order, Elovich, and intraparticle diffusion kinetic models were applied. The best trend line fits the linearized models, and R^2 values are demonstrated in Figure 11, while Table 6 represents the correlation factor and the obtained model's constants.
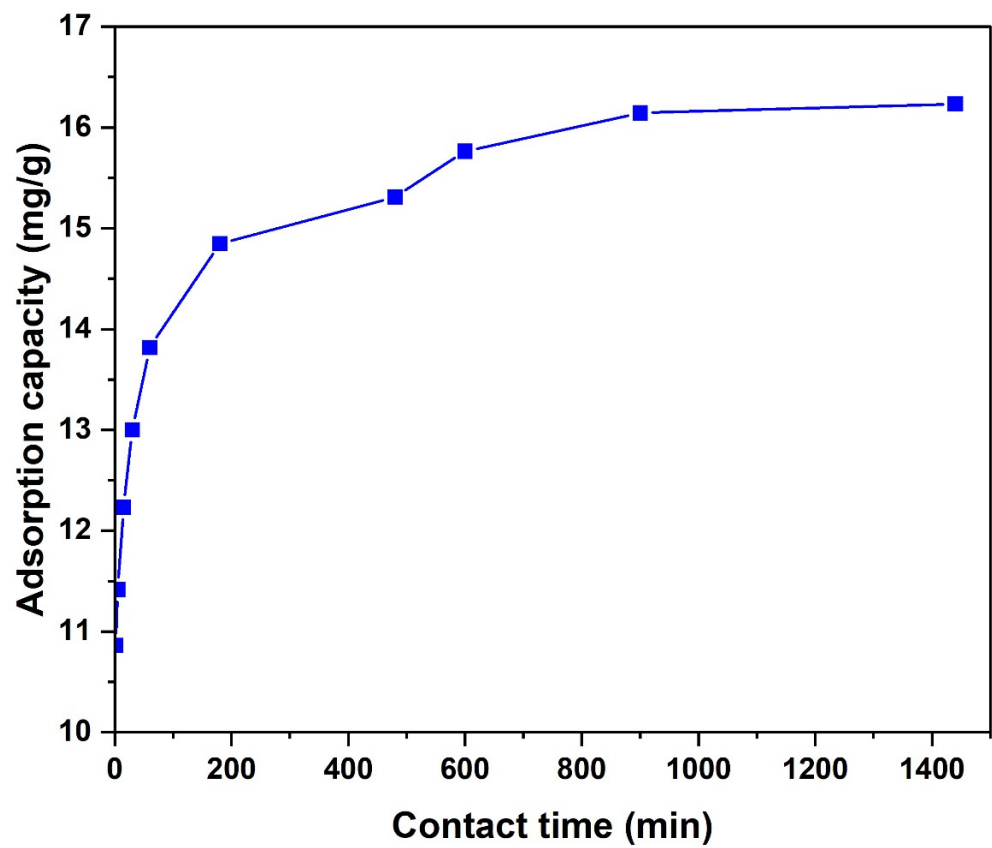
Figure 10. The relation between time and phosphate adsorption on AC/MgAl-3.
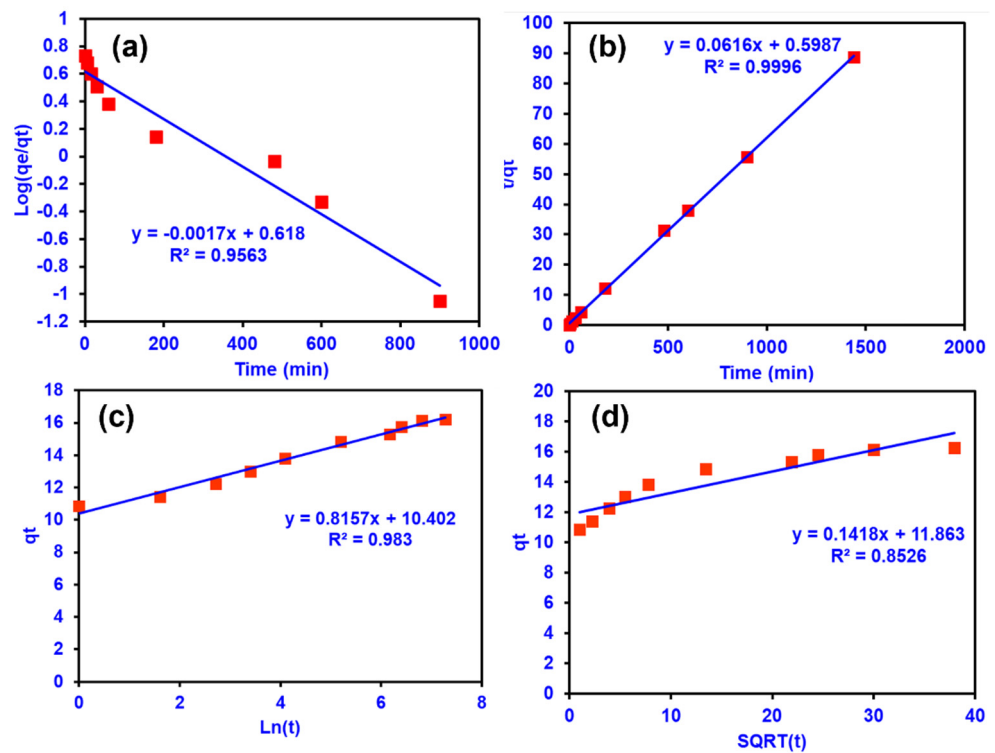

Figure 11. Kinetic models of phosphate adsorption on AC/MgAl-3 (**a**) the pseudo-first-order model, (**b**) the pseudo-second-order model, (**c**) the Elovich model, (**d**) the intraparticle diffusion model.

Table 6. Kinetics model parameters of phosphate removal by AC/MgAl-3.

Kinetic Model	Values
q_{exp} (mg/g)	16.2325
Pseudo-first order	
$q_{e,\text{calc}}$ (mg/g)	4.14954
k_1 (min^{-1})	0.00392
R^2	0.9563
Pseudo-second order	
$q_{e,\text{calc}}$ (mg/g)	16.2338
k_2 (g·mg^{-1}·min^{-1})	0.00634
R^2	0.9996
Elovich model	
α	281680
β	1.22594
R^2	0.983

The interpretation of these models confirmed that the adsorption of phosphate onto AC/MgAl-3 follows the pseudo-second-order kinetics as observed from Regression coefficient values R^2 = 0.9996 as shown in Figure 11b. The compliance with the pseudo-second-order model suggests a chemisorption process between phosphate and the LDH structure. In contrast, the pseudo-first order was not in compliance with the kinetic as confirmed from Figure 11a and R^2 value (0.956). The Elovich model is used to describe the highly heterogeneous surfaces. It can be noticed from Figure 11c and R^2 value (0.983) that the Elovich model has good agreement with the kinetic data. These results imply that the adsorbent surface is heterogeneous, and some information can be extracted from the Elovich constants.

The initial adsorption rate of the Elovich model (α) was 218,680 mg/g/min indicating the very fast adsorption at the beginning of the adsorption process. Another essential parameter: is the Elovich model intercept term ($1/\beta \ln(\alpha\beta)$). This term provides the adsorption amount after 1 min of adsorption (i.e., when ln(t) = zero). For phosphate removal by AC/MgAl-3, this parameter equals 10.4 mg/g. For an adsorption capacity of 16.2 mg/g, about 62.4% occurred after 1 min of adsorption, indicating the very fast kinetics at the beginning of the removal process. Figure 11d elucidates the single-step intra-particle diffusion. According to the trend line fit and R^2 value (0.853), the single step intra-particle diffusion does not fit the experimental kinetic data. Usually, the intra-particle diffusion model is used to investigate the adsorption limiting step [56]. By plotting the data q_t versus $SQRT(t)$, if the data has a straight line and passes through zero, the intra-particle diffusion is the adsorption limiting step, otherwise, the adsorption limiting step is more than the adsorption limiting step controlling the removal process. As confirmed in Figure 11d, the kinetic data did not form a straight line and did not pass through zero. Hence, it is known that the intra-particle is not the controlling mechanism.

Moreover, these results also suggest that the boundary layer diffusion controls the adsorption process to some extent. Splitting the intra-particle diffusion data into three segments produces three straight lines, and the result is illustrated in Figure 12. Step 1 represents the boundary layer diffusion of phosphate ions onto the active vacant adsorption sites on the surface of the adsorbent. This step occurs in the first 30 min and represents about 80.1% of the total adsorption capacity. In step 2, the adsorption took place within the micropores and mesoporous structure of the adsorbent. This step took 570 min to complete and represents about 17% of the total adsorption capacity. In the last step (step 3), phosphate ions get adsorbed in the macropores of the adsorbent until reaching equilibrium. This step is very slow and takes around 600 min to complete. Step 3 is responsible for approximately

2.9% of the total adsorption capacity. The factors of the three-step intra-particle diffusion are tabulated in Table 7.
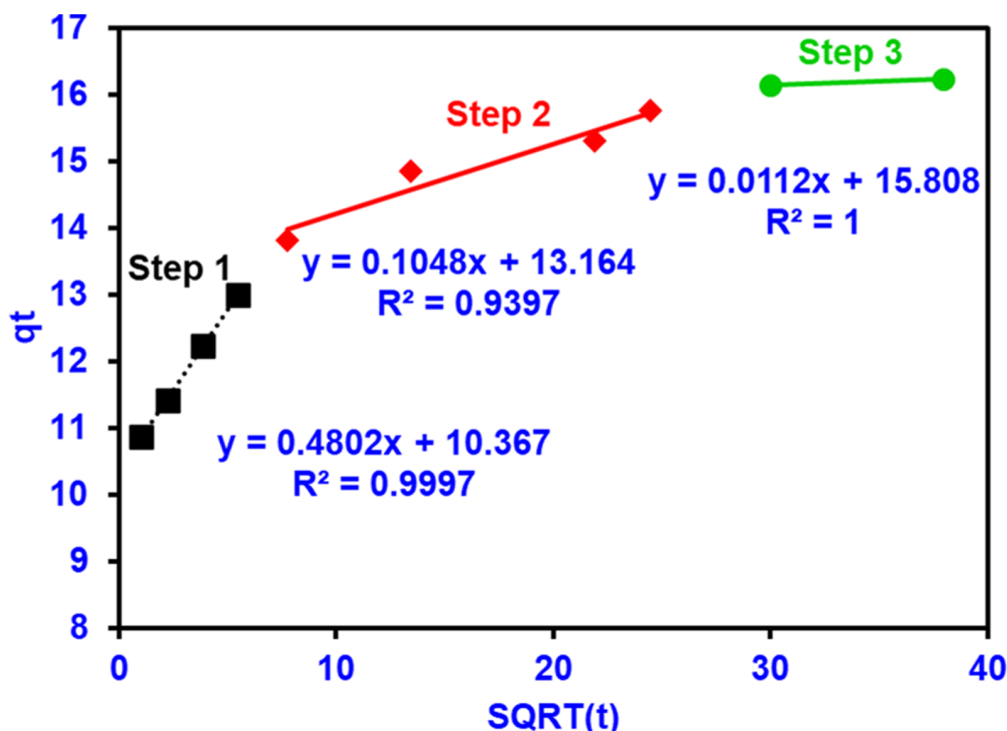

Figure 12. Three-steps intraparticle diffusion for phosphate removal on AC/MgAl-3.

Table 7. Detailed factors of the three-step intra-particle diffusion.

Step	K_{ip}	c	R^2
1	0.4802	10.367	0.9997
2	0.1048	13.164	0.9397
3	0.0112	15.808	1

3.7. Thermodynamics and Effect of Temperature

The thermodynamic factors, including ΔH°, ΔS°, and ΔG° calculated for phosphate adsorption in a temperature range between 22 and 60 °C are given in Table 8. The negative values of ΔG° suggest that the adsorption of phosphate ions by AC/MgAl-3 is a spontaneous and feasible process. The magnitude of the negative value of ΔG° is increasing with temperature implying an endothermic adsorption process. This is confirmed by the positive value of ΔH° (7.64 KJ/mol). The negative or positive value of ΔS° indicates the degree of freedom of pollutant particles at the solid-liquid interface. In our case, the ΔS° was positive (31.15 J/mol/K), suggesting the increase in phosphate ions' randomness and degree of freedom at the adsorbent interface [66]. These results indicate that removing phosphate ions by AC/MgAl-3 is a favorable adsorption process.

Table 8. Thermodynamic parameters of phosphate adsorption on AC/MgAl-3.

Temperature (K)	ΔG° (KJ/mol)	ΔS° (J/mol/K)	ΔH° (KJ/mol)
295	−1.15		
313	−2.17		
323	−2.47	31.15	7.64
333	−2.66		

Figure 13 illustrates the effect of temperature on phosphate removal by AC/MgAl-3 at four different temperatures 295, 313, 323, and 333 K. According to Figure 13, the adsorption capacity of phosphate was gradually increased with increasing temperatures. Meanwhile, the adsorption capacity was 16.23 mg/g at 295 K and 18.1 mg/g at 333 K. The increased adsorption capacity with temperature suggests an endothermic adsorption process confirming the thermodynamic analysis results. This trend might be attributed to the fact that rising temperatures increase the mobility of phosphate ions toward the adsorbent surface and internal pores of the adsorbent. Hence, the adsorption capacity was slightly increasing.
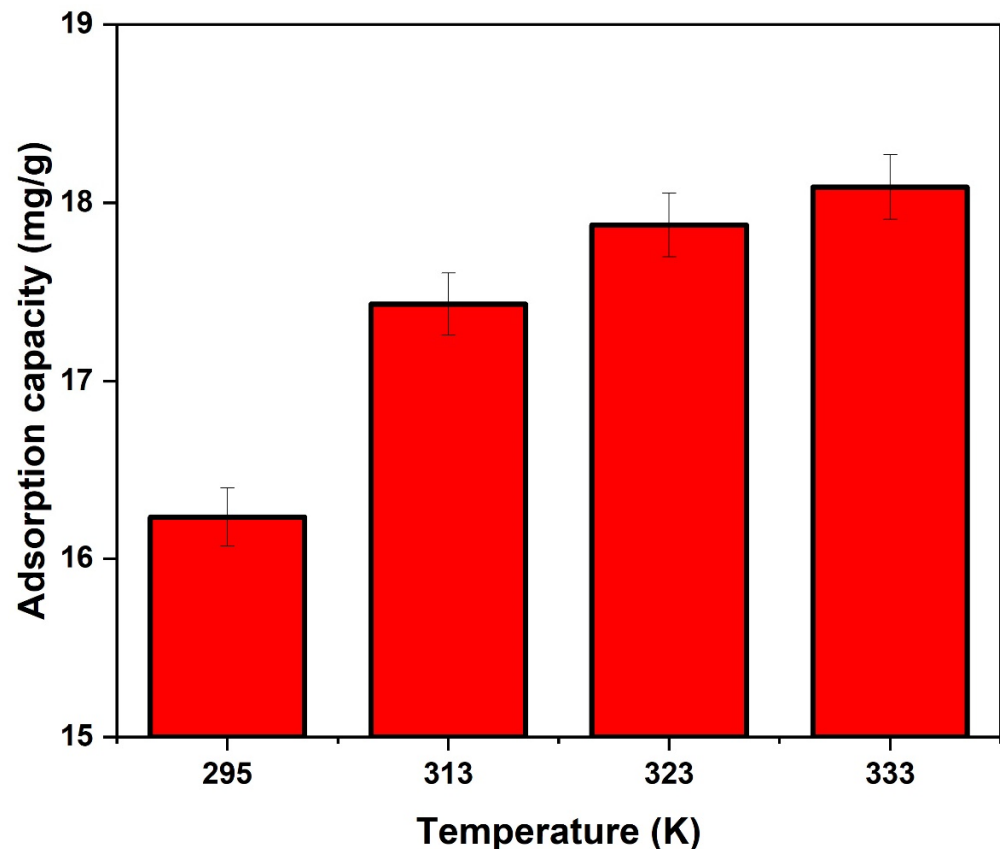

Figure 13. Effect of temperature on phosphate adsorption using AC/MgAl-3.

3.8. EDS and FT-IR Analysis of AC/MgAl-3 after Phosphate Adsorption

The AC/MgAl-3 composite elemental composition was examined after phosphate adsorption through EDS analysis, and elemental mapping is presented in Figure 14. The EDS spectrum shows the presence of phosphorous signals in the sample, which confirms the adsorption of phosphate ions onto the AC/MgAl-3 material surface.

FT-IR analysis was carried out on AC/MgAl-3 adsorbent to gain insights into phosphate adsorption mechanisms between adsorbent and adsorbate. Figure 15 displays the FT-IR spectra of AC/MgAl-3 composite before and after phosphate adsorption. The broad adsorption at 3484 cm^{-1} is assigned to –OH stretching vibrations owing to the structural -OH and interlayer water molecules [27]. It should be noted that the stretching vibration of -OH functional groups shifted from 3484 cm^{-1} to 3471 cm^{-1}, implying the involvement of -OH in the adsorption process. The peak is located at 1635 cm^{-1} due to the bending vibration of the water molecules in the LDH interlayer.
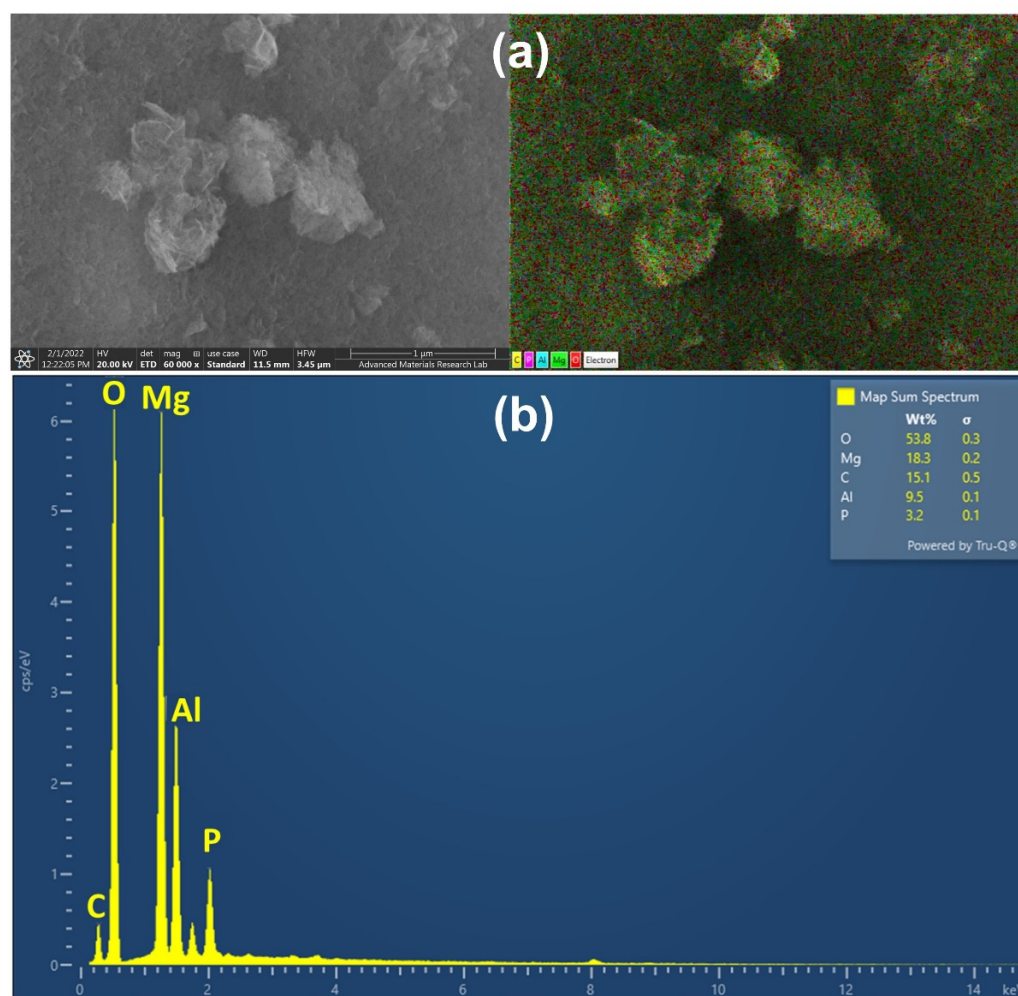
Figure 14. The (**a**) SEM, and (**b**) EDS analysis of AC/MgAl-3 LDH after phosphate adsorption.

The peak at 1387 cm^{-1} is assigned to NO_3^- in the interlayer [27,67]. A strong asymmetry vibration peak of the P-O bond at 1085 cm^{-1} indicated that phosphate was strongly adsorbed by metal oxide surface (Mg-O and Al-O) through potentially monodentate and bidentate formation inner-sphere surface complexes. The peaks in the lower wavenumber region (400–800 cm) correspond to M-OH vibrations and O-M-O stretching (where M = Mg and Al) [30,68]. These results were well corroborated with the typical character of LDHs, which had some easily exchangeable interlayer anions. The results indicate that several phosphate adsorption mechanisms could be anticipated. The phosphate adsorption mechanism onto the AC/MgAl-3 composites mainly occurred via phosphate ion exchange with the interlayer NO_3^-, electrostatic interaction between positively charged metal oxide surfaces with negatively charged phosphate ions, as well as the inner-sphere surface complexation process via ligand exchange.
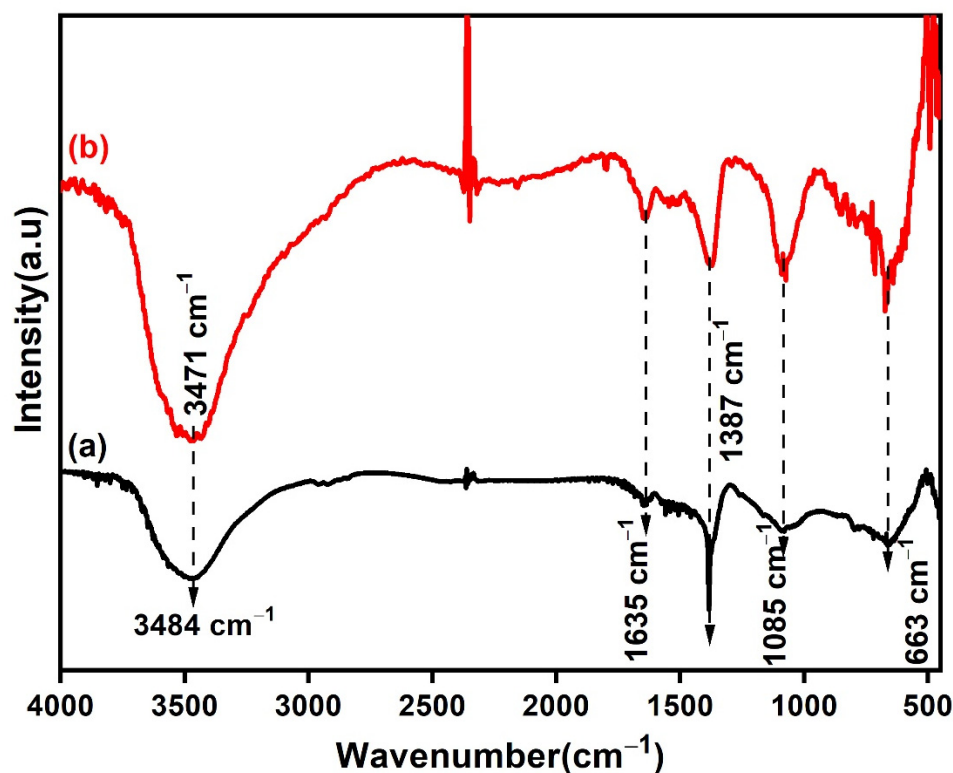
Figure 15. FT-IR spectra of AC/MgAl-3 before (**a**), and after (**b**) phosphate adsorption.

4. Conclusions

In the current study, the AC/MgAl LDH composites as a new effective and low-cost adsorbent was prepared by the co-precipitation method for the removal of phosphate ions from aqueous solutions. The influence of (Mg + Al) loading (5 wt%, 10 wt%, and 15 wt%) onto the AC on the removal of phosphate from water was investigated. The morphology, textural properties, and surface chemistry of the adsorbent was investigated by BET, XRF, FT-IR, XRD, EDS, and FESEM, and the results demonstrated the successful doping of MgAl onto the surface of the AC. Moreover, the MgAl doping was found to improve the surface and chemical properties of the raw AC toward phosphate removal. The adsorption results illustrated a significant improvement in phosphate removal by increasing the (Mg + Al) metal loading with a maximum Langmuir adsorption capacity of 337.2 mg/g at pH 6.3 using 15 wt% of MgAl onto the surface of the AC. It is confirmed that phosphate adsorption onto AC/MgAl-3 follows the pseudo-second order kinetics with a correlation coefficient of more than 0.999. The initial solution pH was found to influence the adsorption process significantly, with a maximum removal at pH 2.3. According to the spent adsorbent characterizations, the phosphate removal by AC/MgAl-3 is dominated by electrostatic attraction, ion exchange, and formation of surface inner-sphere complex. The influence of temperature and thermodynamic investigations elucidated that phosphate removal by AC/MgAl-3 is an endothermic, spontaneous, and feasible adsorption process. Therefore, modifying the AC with MgAl LDH is a promising and applicable material for removing phosphate ions from wastewater streams.

Author Contributions: A.K.A.K.: Writing, Original Draft, Conceptualization; Data curation; Formal analysis, F.D.: Supervision, Conceptualization. I.W.A.: Writing; Conceptualization; Data curation; review & editing. A.C.: Writing, review & editing, Methodology, Investigation. M.A.A.: Visualization, Supervision, Conceptualization. All authors have read and agreed to the published version of the manuscript.

Conflicts of Interest: The authors declare that they have no known competing financial interest or personal relationships that could have appeared to influence the work reported in this paper.

References

1. Abou-Shady, A.; El-Araby, H. Electro-agric, a novel environmental engineering perspective to overcome the global water crisis via marginal water reuse. *Nat. Hazards Res.* **2021**, *1*, 202–226. [CrossRef]
2. Almanassra, I.W.; Mckay, G.; Kochkodan, V.; Atieh, M.A.; Al-Ansari, T. A state of the art review on phosphate removal from water by biochars. *Chem. Eng. J.* **2021**, *409*, 128211. [CrossRef]
3. Ji, X.; Ye, C.; Zhou, J.; He, K.; Zhu, R.; Xiang, H.; Liu, J.; Xie, Z.; Liao, B. Study on the microscale structure and barrier mechanism of magnesium phosphate cement modified with fly ash cutoff walls for lead pollution in groundwater. *Constr. Build. Mater.* **2021**, *308*, 124994. [CrossRef]
4. Ihsanullah, I.; Khan, M.T.; Zubair, M.; Bilal, M.; Sajid, M. Removal of pharmaceuticals from water using sewage sludge-derived biochar: A review. *Chemosphere* **2022**, *289*, 133196. [CrossRef]
5. Chen, Y.; Long, J.; Chen, S.; Xie, Y.; Xu, Z.; Ning, Z.; Zhang, G.; Xiao, T.; Yu, M.; Ke, Y.; et al. Multi-step purification of electrolytic manganese residue leachate using hydroxide sedimentation, struvite precipitation, chlorination and coagulation: Advanced removal of manganese, ammonium, and phosphate. *Sci. Total Environ.* **2022**, *805*, 150237. [CrossRef]
6. Yu, W.; Gan, Z.; Wang, J.; Zhao, Y.; Han, J.; Fang, L.; Wei, X.; Qiu, Z.; Zhu, B. A novel negatively charged nanofiltration membrane with improved and stable rejection of Cr (VI) and phosphate under different pH conditions. *J. Membr. Sci.* **2021**, *639*, 119756. [CrossRef]
7. Dong, H.; Lin, T.; SenGupta, A.K. Field validation of multifunctional ion exchange process for reverse osmosis pretreatment and phosphate recovery during impaired water reuse. *J. Water Process Eng.* **2020**, *36*, 101347. [CrossRef]
8. Almanassra, I.W.; Kochkodan, V.; Mckay, G.; Atieh, M.A.; Al-Ansari, T. Kinetic and thermodynamic investigations of surfactants adsorption from water by carbide-derived carbon. *J. Environ. Sci. Health Part A* **2021**, *56*, 1206–1220. [CrossRef]
9. Almanassra, I.W.; Kochkodan, V.; Mckay, G.; Atieh, M.A.; Al-Ansari, T. Review of phosphate removal from water by carbonaceous sorbents. *J. Environ. Manag.* **2021**, *287*, 112245. [CrossRef]
10. Zhang, B.; Xu, L.; Zhao, Z.; Peng, S.; Yu, C.; Zhang, X.; Zong, Y.; Wu, D. Enhanced phosphate removal by nano-lanthanum hydroxide embedded silica aerogel composites: Superior performance and insights into specific adsorption mechanism. *Sep. Purif. Technol.* **2021**, *285*, 120365. [CrossRef]
11. Moshi, A.O.; Wild, A.; Greenland, D.J. Effect of organic matter on the charge and phosphate adsorption characteristics of Kikuyu red clay from Kenya. *Geoderma* **1974**, *11*, 275–285. [CrossRef]
12. Nazarian, R.; Desch, R.J.; Thiel, S.W. Kinetics and equilibrium adsorption of phosphate on lanthanum oxide supported on activated carbon. *Colloids Surf. Physicochem. Eng. Asp.* **2021**, *624*, 126813. [CrossRef]
13. Huang, Q.; Zhao, Z.; Chen, W. Effects of several low-molecular weight organic acids and phosphate on the adsorption of acid phosphatase by soil colloids and minerals. *Chemosphere* **2003**, *52*, 571–579. [CrossRef]
14. Goscianska, J.; Ptaszkowska-Koniarz, M.; Frankowski, M.; Franus, M.; Panek, R.; Franus, W. Removal of phosphate from water by lanthanum-modified zeolites obtained from fly ash. *J. Colloid Interface Sci.* **2018**, *513*, 72–81. [CrossRef] [PubMed]
15. Wang, Y.; Yang, Q.; Huang, H. Effective adsorption of trace phosphate and aluminum in realistic water by carbon nanotubes and reduced graphene oxides. *Sci. Total Environ.* **2019**, *662*, 1003–1011. [CrossRef]
16. Mekonnen, D.T.; Alemayehu, E.; Lennartz, B. Removal of phosphate ions from aqueous solutions by adsorption onto leftover coal. *Water* **2020**, *12*, 1381. [CrossRef]
17. Hakkar, M.; Ezzahra Arhouni, F.; Mahrou, A.; Bilal, E.; Bertau, M.; Roy, A.; Steiner, G.; Haneklaus, N.; Mazouz, H.; Boukhair, A.; et al. Enhancing rare earth element transfer from phosphate rock to phosphoric acid using an inexpensive fly ash additive. *Miner. Eng.* **2021**, *172*, 107166. [CrossRef]
18. Gayathiri, M.; Pulingam, T.; Lee, K.T.; Sudesh, K. Activated carbon from biomass waste precursors: Factors affecting production and adsorption mechanism. *Chemosphere* **2022**, *294*, 133764. [CrossRef]
19. Zhang, Q.L.; Lin, Y.C.; Chen, X.; Gao, N.Y. A method for preparing ferric activated carbon composites adsorbents to remove arsenic from drinking water. *J. Hazard. Mater.* **2007**, *148*, 671–678. [CrossRef]
20. Zhu, Y.; Xiong, C.; Song, S.; Le, Z.; Jiang, S. Coordination-driven synthesis of perfected π-conjugated graphitic carbon nitride with efficient charge transfer for oxygen activation and gas purification. *J. Colloid Interface Sci.* **2019**, *538*, 237–247. [CrossRef]
21. Humbert, H.; Gallard, H.; Suty, H.; Croué, J. Natural organic matter (NOM) and pesticides removal using a combination of ion exchange resin and powdered activated carbon (PAC). *Water Res.* **2008**, *42*, 1635–1643. [CrossRef] [PubMed]
22. Duan, D.; Feng, Z.; Zhang, Y.; Zhou, T.; Xu, Z.; Wang, Q.; Zhao, Y.; Wang, C.; Ruan, R. Corncob pyrolysis: Improvement in hydrocarbon group types distribution of bio oil from co-catalysis over HZSM-5 and activated carbon. *Waste Manag.* **2022**, *141*, 8–15. [CrossRef] [PubMed]

23. Mong, G.R.; Chong, W.W.F.; Nor, S.A.M.; Ng, J.; Chong, C.T.; Idris, R.; Too, J.; Chiong, M.C.; Abas, M.A. Pyrolysis of waste activated sludge from food manufacturing industry: Thermal degradation, kinetics and thermodynamics analysis. *Energy* **2021**, *235*, 121264. [CrossRef]

24. Zubair, M.; Aziz, H.A.; Ihsanullah, I.; Ahmad, M.A.; Al-Harthi, M.A. Biochar supported CuFe layered double hydroxide composite as a sustainable adsorbent for efficient removal of anionic azo dye from water. *Environ. Technol. Innov.* **2021**, *23*, 101614. [CrossRef]

25. Gupta, N.K.; Saifuddin, M.; Kim, S.; Kim, K.S. Microscopic, spectroscopic, and experimental approach towards understanding the phosphate adsorption onto Zn–Fe layered double hydroxide. *J. Mol. Liq.* **2020**, *297*, 111935. [CrossRef]

26. Santos, L.C.; da Silva, A.F. Mg-Fe layered double hydroxide with chloride intercalated: Synthesis, characterization and application for efficient nitrate removal. *Environ. Sci. Pollut. Res.* **2020**, *27*, 5890–5900. [CrossRef]

27. Liu, C.; Zhang, M.; Pan, G.; Lundehøj, L.; Nielsen, U.G.; Shi, Y.; Hansen, H.C.B. Phosphate capture by ultrathin MgAl layered double hydroxide nanoparticles. *Appl. Clay Sci.* **2019**, *177*, 82–90. [CrossRef]

28. Li, H.; Cui, S.; Tan, Y.; Peng, Y.; Gao, X.; Yang, X.; Ma, Y.; He, X.; Fan, B.; Yang, S.; et al. Synergistic effects of ball-milled biochar-supported exfoliated LDHs on phosphate adsorption: Insights into role of fine biochar support. *Environ. Pollut.* **2022**, *294*, 118592. [CrossRef]

29. Rahman, S.; Navarathna, C.M.; Das, N.K.; Alchouron, J.; Reneau, P.; Stokes, S.; Thirumalai, R.V.; Perez, F.; Hassan, E.B.; Mohan, D.; et al. High capacity aqueous phosphate reclamation using Fe/Mg-layered double hydroxide (LDH) dispersed on biochar. *J. Colloid Interface Sci.* **2021**, *597*, 182–195. [CrossRef]

30. Li, R.; Wang, J.J.; Zhou, B.; Awasthi, M.K.; Ali, A.; Zhang, Z.; Gaston, L.A.; Lahori, A.H.; Mahar, A. Enhancing phosphate adsorption by Mg/Al layered double hydroxide functionalized biochar with different Mg/Al ratios. *Sci. Total Environ.* **2016**, *559*, 121–129. [CrossRef]

31. Lin, X.; Wu, J.; Fan, J.; Qian, W.; Zhou, X.; Qian, C.; Jin, X.; Wang, L.; Bai, J.; Ying, H. Adsorption of butanol from aqueous solution onto a new type of macroporous adsorption resin: Studies of adsorption isotherms and kinetics simulation. *J. Chem. Technol. Biotechnol.* **2012**, *87*, 924–931. [CrossRef]

32. Langmuir, I. The constitution and fundamental properties of solids and liquids. Part I. Solids. *J. Am. Chem. Soc.* **1916**, *38*, 2221–2295. [CrossRef]

33. Freundlich, H. Over the adsorption in solution. *J. Phys. Chem.* **1906**, *57*, 1100–1107.

34. Sips, R. On the structure of a catalyst surface. *J. Chem. Phys.* **1948**, *16*, 490–495. [CrossRef]

35. Lima, É.C.; Adebayo, M.A.; Machado, F.M. Kinetic and equilibrium models of adsorption. In *Carbon nanomaterials as Adsorbents for Environmental and Biological Applications*; Springer: Berlin/Heidelberg, Germany, 2015; pp. 33–69.

36. Foo, K.Y.; Hameed, B.H. Insights into the modeling of adsorption isotherm systems. *Chem. Eng. J.* **2010**, *156*, 2–10. [CrossRef]

37. Almasri, D.A.; Saleh, N.B.; Atieh, M.A.; McKay, G.; Ahzi, S. Adsorption of phosphate on iron oxide doped halloysite nanotubes. *Sci. Rep.* **2019**, *9*, 3232. [CrossRef]

38. Bu, X.; Xie, G.; Peng, Y.; Chen, Y. Kinetic modeling and optimization of flotation process in a cyclonic microbubble flotation column using composite central design methodology. *Int. J. Miner. Process.* **2016**, *157*, 175–183. [CrossRef]

39. Polat, M.; Chander, S. First-order flotation kinetics models and methods for estimation of the true distribution of flotation rate constants. *Int. J. Miner. Process.* **2000**, *58*, 145–166. [CrossRef]

40. Yuh-Shan, H. Citation review of Lagergren kinetic rate equation on adsorption reactions. *Scientometrics* **2004**, *59*, 171–177. [CrossRef]

41. Ho, Y.; McKay, G. Pseudo-second order model for sorption processes. *Process Biochem.* **1999**, *34*, 451–465. [CrossRef]

42. Ho, Y.S.; McKay, G. The kinetics of sorption of divalent metal ions onto sphagnum moss peat. *Water Res.* **2000**, *34*, 735–742. [CrossRef]

43. Weber Jr, W.J.; Morris, J.C. Kinetics of adsorption on carbon from solution. *J. Sanit. Eng. Div.* **1963**, *89*, 31–59. [CrossRef]

44. Zuo, J.; Wang, J.; Jiang, Y. Macro/meso failure behavior of surrounding rock in deep roadway and its control technology. *Int. J. Coal Sci. Technol.* **2019**, *6*, 301–319. [CrossRef]

45. Sing, K.S. Reporting physisorption data for gas/solid systems with special reference to the determination of surface area and porosity (Recommendations 1984). *Pure Appl. Chem.* **1985**, *57*, 603–619. [CrossRef]

46. Alagha, O.; Manzar, M.S.; Zubair, M.; Anil, I.; Mu'azu, N.D.; Qureshi, A. Magnetic Mg-Fe/LDH intercalated activated carbon composites for nitrate and phosphate removal from wastewater: Insight into behavior and mechanisms. *Nanomaterials* **2020**, *10*, 1361. [CrossRef]

47. Li, X.; Xu, K.; Zhang, Y.; Sun, C.; He, Y. Optical determination of lead chrome green in green tea by fourier transform infrared (FT-IR) transmission spectroscopy. *PLoS ONE* **2017**, *12*, e0169430. [CrossRef]

48. Vickers, N.J. Animal communication: When i'm calling you, will you answer too? *Curr. Biol.* **2017**, *27*, R713–R715. [CrossRef]

49. Hatami, H.; Fotovat, A.; Halajnia, A. Comparison of adsorption and desorption of phosphate on synthesized Zn-Al LDH by two methods in a simulated soil solution. *Appl. Clay Sci.* **2018**, *152*, 333–341. [CrossRef]

50. Frost, R.L.; Kloprogge, J.T. Infrared emission spectroscopic study of brucite. *Spectrochim. Acta Part A: Mol. Biomol. Spectroscopy* **1999**, *55*, 2195–2205. [CrossRef]

51. Richardson, M.C.; Braterman, P.S. Infrared Spectra of Oriented and Nonoriented Layered Double Hydroxides in the Range from 4000 to 250 cm-1, with Evidence for Regular Short-Range Order in a Synthetic Magnesium−Aluminum LDH with Mg:Al = 2:1 but Not with Mg:Al= 3:1. *J. Phys. Chem. C* **2007**, *111*, 4209–4215. [CrossRef]

52. Zhang, M.; Gao, B.; Yao, Y.; Inyang, M. Phosphate removal ability of biochar/MgAl-LDH ultra-fine composites prepared by liquid-phase deposition. *Chemosphere* **2013**, *92*, 1042–1047. [CrossRef] [PubMed]

53. Wang, S.; Liu, C.H.; Wang, M.K.; Chuang, Y.H.; Chiang, P.N. Arsenate adsorption by Mg/Al–NO3 layered double hydroxides with varying the Mg/Al ratio. *Appl. Clay Sci.* **2009**, *43*, 79–85. [CrossRef]

54. Gorzin, F. Bahri Rasht Abadi, M M Adsorption of Cr (VI) from aqueous solution by adsorbent prepared from paper mill sludge: Kinetics and thermodynamics studies. *Adsorpt. Sci. Technol.* **2018**, *36*, 149–169. [CrossRef]

55. Lu, J.; Liu, H.; Zhao, X.; Jefferson, W.; Cheng, F.; Qu, J. Phosphate removal from water using freshly formed Fe–Mn binary oxide: Adsorption behaviors and mechanisms. *Colloids Surf. Physicochem. Eng. Asp.* **2014**, *455*, 11–18. [CrossRef]

56. Chubar, N.I.; Kanibolotskyy, V.A.; Strelko, V.V.; Gallios, G.G.; Samanidou, V.F.; Shaposhnikova, T.O.; Milgrandt, V.G.; Zhuravlev, I.Z. Adsorption of phosphate ions on novel inorganic ion exchangers. *Colloids Surf. Physicochem. Eng. Asp.* **2005**, *255*, 55–63. [CrossRef]

57. Cardenas Peña, A.M.; Ibañez Cornejo, J.G.; Vásquez Medrano, R.C. Determination of the point of zero charge for electrocoagulation precipitates from an iron anode. *Int. J. Electrochem. Sci.* **2012**, *7*, 6142–6153.

58. Jung, K.; Jeong, T.; Hwang, M.; Kim, K.; Ahn, K. Phosphate adsorption ability of biochar/Mg–Al assembled nanocomposites prepared by aluminum-electrode based electro-assisted modification method with MgCl2 as electrolyte. *Bioresour. Technol.* **2015**, *198*, 603–610. [CrossRef]

59. Chowdhury, S.R.; Yanful, E.K. Arsenic and chromium removal by mixed magnetite–maghemite nanoparticles and the effect of phosphate on removal. *J. Environ. Manag.* **2010**, *91*, 2238–2247. [CrossRef]

60. Bernardo, M.P.; Ribeiro, C. [Mg-Al]-LDH and [Zn-Al]-LDH as matrices for removal of high loadings of phosphate. *Mater. Res.* **2018**, *21*, 1–9. [CrossRef]

61. Lin, Z.; Chen, J. Magnetic Fe_3O_4@MgAl-LDH@La$(OH)_3$ composites with a hierarchical core-shell structure for phosphate removal from wastewater and inhibition of labile sedimentary phosphorus release. *Chemosphere* **2021**, *264*, 128551. [CrossRef]

62. Novillo, C.; Guaya, D.; Allen-Perkins Avendaño, A.; Armijos, C.; Cortina, J.L.; Cota, I. Evaluation of phosphate removal capacity of Mg/Al layered double hydroxides from aqueous solutions. *Fuel* **2014**, *138*, 72–79. [CrossRef]

63. Karthikeyan, P.; Meenakshi, S. Synthesis and characterization of Zn–Al LDHs/activated carbon composite and its adsorption properties for phosphate and nitrate ions in aqueous medium. *J. Mol. Liq.* **2019**, *296*, 111766. [CrossRef]

64. Hu, F.; Wang, M.; Peng, X.; Qiu, F.; Zhang, T.; Dai, H.; Liu, Z.; Cao, Z. High-efficient adsorption of phosphates from water by hierarchical CuAl/biomass carbon fiber layered double hydroxide. *Colloids Surf. Physicochem. Eng. Asp.* **2018**, *555*, 314–323. [CrossRef]

65. Lalley, J.; Han, C.; Li, X.; Dionysiou, D.D.; Nadagouda, M.N. Phosphate adsorption using modified iron oxide-based sorbents in lake water: Kinetics, equilibrium, and column tests. *Chem. Eng. J.* **2016**, *284*, 1386–1396. [CrossRef]

66. Benhiti, R.; Ichou, A.A.; Zaghloul, A.; Carja, G.; Zerbet, M.; Sinan, F.; Chiban, M. Kinetic, isotherm, thermodynamic and mechanism investigations of dihydrogen phosphate removal by MgAl-LDH. *Nanotechnol. Environ. Eng.* **2021**, *6*, 16. [CrossRef]

67. Zhang, Q.; Ji, F.; Zhao, T.; Shen, Q.; Fang, D.; Kuang, L.; Jiang, L.; Ding, S. Systematic screening of layered double hydroxides for phosphate removal and mechanism insight. *Appl. Clay Sci.* **2019**, *174*, 159–169. [CrossRef]

68. Tan, X.; Liu, S.; Liu, Y.; Gu, Y.; Zeng, G.; Cai, X.; Yan, Z.; Yang, C.; Hu, X.; Chen, B. One-pot synthesis of carbon supported calcined-Mg/Al layered double hydroxides for antibiotic removal by slow pyrolysis of biomass waste. *Sci. Rep.* **2016**, *6*, 39691. [CrossRef]